Draft version October 26, 2016
Preprint typeset using LaTeX style emulateapj v. 5/2/11

arXiv:1602.03545v4 [astro-ph.HE] 25 Oct 2016

ON THE RATE AND ON THE GRAVITATIONAL WAVE EMISSION OF SHORT AND LONG GRBS

R. Ruffini[1,2,3,4], J. Rodriguez[1,2], M. Muccino[1,2], J. A. Rueda[1,2,4], Y. Aimuratov[1,2], U. Barres de Almeida[4,5], L. Becerra[1,2], C. L. Bianco[1,2], C. Cherubini[6,7], S. Filippi[6,7], D. Gizzi[1], M. Kovacevic[1,2,3], R. Moradi[1,2], F. G. Oliveira[1,2,3], G. B. Pisani[1,2], Y. Wang[1,2]

(Dated: October 26, 2016)
Draft version October 26, 2016

ABSTRACT

GRBs, traditionally classified as "long" and "short", have been often assumed, till recently, to originate from a single black hole (BH) with an ultrarelativistic jetted emission. There is evidence that both long and short bursts have as progenitors merging and/or accreting binaries, each composed by a different combination of carbon-oxygen cores (CO_{core}), neutron stars (NSs), BHs and white dwarfs (WDs). Consequently, the traditional long bursts have been sub-classified as (I) X-ray flashes (XRFs), (II) binary-driven hypernovae (BdHNe), and (III) BH-supernovae (BH-SNe). They are framed within the induced gravitational collapse (IGC) paradigm which envisages as progenitor a tight binary composed of a CO_{core} and a NS or BH companion. The SN explosion of the CO_{core}, originating a new NS (νNS), triggers a hypercritical accretion process onto the companion NS or BH. If the accretion is not sufficient for the NS to reach its critical mass, an XRF occurs, leading to a νNS-NS system. Instead, when the BH is already present or formed by the hypercritical accretion, a BdHN occurs, leading to a νNS-BH system. Similarly, the traditional short bursts, originating in NS-NS mergers, are sub-classified as (IV) short gamma-ray flashes (S-GRFs) and (V) short GRBs (S-GRBs), respectively when the merging process does not lead or leads to BH formation. Two additional families are (VI) ultra-short GRBs (U-GRBs) and (VII) gamma-ray flashes (GRFs), respectively formed in νNS-BH and NS-WD mergers. We use the estimated occurrence rate of the above sub-classes to assess the gravitational wave emission in the merging process and its detectability by Advanced LIGO, Advanced Virgo, eLISA, and resonant bars.

Subject headings: gamma-ray burst: general — gravitational waves — black hole physics — stars: neutron — white dwarfs — binaries: general

1. INTRODUCTION

Thanks to the extensive observations carried out by γ-ray telescopes, such as AGILE, BATSE, BeppoSAX, *Fermi*, *HETE-II*, *INTEGRAL*, Konus/WIND and *Swift*, our understanding of "long" and "short" gamma-ray burst (GRB) progenitor systems has greatly improved. This has led also to a vast literature devoted to the estimate of their relative occurrence rates, all in general agreement. For long bursts see, e.g., Soderberg et al. (2006); Guetta & Della Valle (2007); Liang et al. (2007); Virgili et al. (2009); Rangel Lemos et al. (2010); Wanderman & Piran (2010); Guetta et al. (2011); Kovacevic et al. (2014); for short bursts see, e.g., Virgili et al. (2011); Wanderman & Piran (2015); and for both long and short bursts see, e.g., Sun et al. (2015); Ruffini et al. (2016).

Our aim in this article is to use the rate of the GRB occurrence to assess the detectability of their associated gravitational wave (GW) emission by the ground-based interferometers Advanced LIGO (hereafter aLIGO) and Advanced Virgo (hereafter AdV), by the space-based interferometer eLISA, as well as by the resonant bars. In order to do this we have to identify the different kinds of GRB progenitors. GRBs, traditionally classified as long and short, have been often assumed, till recently, to originate from a single black hole (BH) with an ultrarelativistic jetted emission. There is today clear evidence (see Ruffini et al. 2016) that both long and short bursts have as progenitors merging and/or accreting binary systems, each composed by a different combination of carbon-oxygen cores (CO_{core}), neutron stars (NSs), black holes (BHs) and white dwarfs (WDs). For each system the initial state and the final state are respectively here referred to as "*in-state*" and "*out-state*".

For the traditional long GRBs, the induced gravitational collapse (IGC) paradigm (Ruffini et al. 2006, 2007, 2008; Izzo et al. 2012; Rueda & Ruffini 2012; Fryer et al. 2014; Ruffini et al. 2015a) proposes as *in-state* a tight binary system composed of a CO_{core} undergoing a supernova (SN) explosion and a companion compact object, e.g. a NS or a BH. The SN explosion triggers hypercritical accretion onto the companion (Ruffini et al. 2016). They are classified into three sub-classes (Ruffini et al. 2016):

I. X-ray flashes (XRFs) with isotropic energy $E_{\rm iso} \lesssim 10^{52}$ erg and rest-frame spectral peak energy $E_{p,i} \lesssim 200$ keV. This class occurs in CO_{core}–NS binaries when the hypercritical accretion onto the NS com-

[1] Dipartimento di Fisica and ICRA, Sapienza Università di Roma, P.le Aldo Moro 5, I–00185 Rome, Italy
[2] ICRANet, P.zza della Repubblica 10, I–65122 Pescara, Italy
[3] Université de Nice Sophia Antipolis, CEDEX 2, Grand Château Parc Valrose, Nice, France
[4] ICRANet-Rio, Centro Brasileiro de Pesquisas Físicas, Rua Dr. Xavier Sigaud 150, 22290–180 Rio de Janeiro, Brazil
[5] Centro Brasileiro de Pesquisas Físicas, Rua Dr. Xavier Sigaud 150, 22290–180 Rio de Janeiro, Brazil
[6] Unit of Nonlinear Physics and Mathematical Modeling, Università Campus Bio-Medico di Roma, Via A. del Portillo 21, I–00128 Rome, Italy
[7] ICRA, Università Campus Bio-Medico di Roma, Via A. del Portillo 21, I–00128 Rome, Italy

Table 1
Summary of the astrophysical aspects of the different GRB sub-classes and of their observational properties. In the first four columns we indicate the GRB sub-classes and their corresponding *in-states* and the *out-states*. In columns 5–8 we list the ranges of $E_{\rm p,i}$ and $E_{\rm iso}$ (rest-frame 1–10^4 keV), $E_{\rm iso,X}$ (rest-frame 0.3–10 keV), and $E_{\rm iso,GeV}$ (rest-frame 0.1–100 GeV). Columns 9 and 10 list, for each GRB sub-class, the maximum observed redshift and the local observed rate $\rho_{\rm GRB}$ obtained in Ruffini et al. (2016).

	Sub-class	*In-state*	*Out-state*	$E_{\rm p,i}$ (MeV)	$E_{\rm iso}$ (erg)	$E_{\rm iso,X}$ (erg)	$E_{\rm iso,Gev}$ (erg)	$z_{\rm max}$	$\rho_{\rm GRB}$ (Gpc^{-3}yr^{-1})
I	XRFs	CO_{core}-NS	νNS-NS	$\lesssim 0.2$	$\sim 10^{48}$–10^{52}	$\sim 10^{48}$–10^{51}	–	1.096	100^{+45}_{-34}
II	BdHNe	CO_{core}-NS	νNS-BH	~ 0.2–2	$\sim 10^{52}$–10^{54}	$\sim 10^{51}$–10^{52}	$\lesssim 10^{53}$	9.3	$0.77^{+0.09}_{-0.08}$
III	BH-SN	CO_{core}-BH	νNS-BH	$\gtrsim 2$	$> 10^{54}$	$\sim 10^{51}$–10^{52}	$\gtrsim 10^{53}$	9.3	$\lesssim 0.77^{+0.09}_{-0.08}$
IV	S-GRFs	NS-NS	MNS	$\lesssim 2$	$\sim 10^{49}$–10^{52}	$\sim 10^{49}$–10^{51}	–	2.609	$3.6^{+1.4}_{-1.0}$
V	S-GRBs	NS-NS	BH	$\gtrsim 2$	$\sim 10^{52}$–10^{53}	$\lesssim 10^{51}$	$\sim 10^{52}$–10^{53}	5.52	$\left(1.9^{+1.8}_{-1.1}\right)\times 10^{-3}$
VI	U-GRBs	νNS-BH	BH	$\gtrsim 2$	$> 10^{52}$	–	–	–	$\gtrsim 0.77^{+0.09}_{-0.08}$
VII	GRFs	NS-WD	MNS	~ 0.2–2	$\sim 10^{51}$–10^{52}	$\sim 10^{49}$–10^{50}	–	2.31	$1.02^{+0.71}_{-0.46}$

panion is not enough to induce gravitational collapse into a BH (Becerra et al. 2016, 2015). Thus, the *out-states* of XRFs are binaries composed of a newly-formed ~ 1.4–$1.5\ M_\odot$ NS (hereafter νNS) born in the SN explosion, and a massive NS (MNS) which accreted matter from the SN ejecta. Their occurrence rate is $\rho_{\rm XRF} = 100^{+45}_{-34}$ Gpc^{-3} yr^{-1} (Ruffini et al. 2016), which is in agreement with those for low-luminous long GRBs (Liang et al. 2007; Virgili et al. 2009; Sun et al. 2015).

II. Binary-driven hypernovae (BdHNe) with $E_{\rm iso} \gtrsim 10^{52}$ erg and $E_{p,i} \gtrsim 200$ keV. BdHNe occur in more compact CO_{core}–NS binaries which leads to a more massive hypercritical accretion onto the NS, hence leading to BH formation. Therefore, the *out-states* of BdHNe are νNS-BH binaries (Becerra et al. 2016; Fryer et al. 2015; Becerra et al. 2015). Their occurrence rate is $\rho_{\rm BdHN} = 0.77^{+0.09}_{-0.08}$ Gpc^{-3} yr^{-1} (Ruffini et al. 2016), which is in agreement with those for high-luminous long GRBs (Wanderman & Piran 2010; Sun et al. 2015).

III. BH-SN with $E_{\rm iso} \gtrsim 10^{54}$ erg and $E_{p,i} \gtrsim 2$ MeV. BH-SN occur in close CO_{core}-BH binaries (Ruffini et al. 2001) in which the hypercritical accretion produces, as *out-states*, a more massive BH and a νNS. Such BH-SN systems correspond to the late evolutionary stages of X-ray binaries, as Cyg X-1 and Cyg X-3 (Giacconi & Ruffini 1978), or micro-quasars (Mirabel & Rodríguez 1998). These systems are here considered a sub-set of the BdHNe. Therefore, in the following we assume the rate of BdHNe as an upper limit to the rate of BH-SNe, i.e. $\rho_{\rm BH-SN} \lesssim 0.77^{+0.09}_{-0.08}$ Gpc^{-3} yr^{-1} (Ruffini et al. 2016).

Similarly, for the traditional short GRBs, the *in-states* are NS-NS or NS-BH merging binaries, as commonly adopted also within the traditional models (see, e.g., Goodman 1986; Paczynski 1986; Eichler et al. 1989; Narayan et al. 1991; Meszaros & Rees 1997; Rosswog et al. 2003; Lee et al. 2004; Berger 2014). They are divided into three sub-classes (Fryer et al. 2015; Ruffini et al. 2015b, 2016):

IV. Short gamma-ray flashes (S-GRFs), with $E_{\rm iso} \lesssim 10^{52}$ erg and $E_{p,i} \lesssim 2$ MeV, occur when no BH is formed in the NS-NS merger, i.e. they lead to a MNS. Their occurrence rate is $\rho_{\rm S-GRF} = 3.6^{+1.4}_{-1.0}$ Gpc^{-3} yr^{-1} (Ruffini et al. 2016), which is in agreement with the estimates obtained from the whole short burst population reported in the literature (Wanderman & Piran 2015; Sun et al. 2015).

V. Authentic short GRBs (S-GRBs), with $E_{\rm iso} \gtrsim 10^{52}$ erg and $E_{p,i} \gtrsim 2$ MeV, occur when a BH is formed in the NS-NS merger. Their occurrence rate is $\rho_{\rm S-GRB} = \left(1.9^{+1.8}_{-1.1}\right)\times 10^{-3}$ Gpc^{-3} yr^{-1} (Ruffini et al. 2016).

VI. Ultra-short GRBs (U-GRBs), a new sub-class of short bursts originating from νNS-BH merging binaries. Such systems are yet unobserved and present a great challenge not only in the present case of high-energy but also possibly in the radio band where they would manifest themselves as pulsar-BH binaries (see, e.g., Tauris et al. 2015, and references therein). They can originate from BdHNe (see II above) or from BH-SN events (see III above). We recall that in Fryer et al. (2015) it is shown that the majority of BdHN *out-states* remain bound. We thus assume as an ansatz that $\rho_{\rm U-GRB} \approx \rho_{\rm BdHN} = 0.77^{+0.09}_{-0.08}$ Gpc^{-3} yr^{-1} (Ruffini et al. 2016).

VII. Gamma-ray flashes (GRFs) have $10^{51} \lesssim E_{\rm iso} \lesssim 10^{52}$ erg and $0.2 \lesssim E_{p,i} \lesssim 2$ MeV. This sub-class of sources originates in NS-WD mergers (Ruffini et al. 2016). These binaries are notoriously very common astrophysical systems (Cadelano et al. 2015) and possible evolutionary scenarios leading to such mergers have been envisaged (see, e.g., Lazarus et al. 2014; Tauris et al. 2000). GRFs form a MNS and not a BH (see Ruffini et al. 2016, for details). Their rate of occurrence is $\rho_{\rm GRF} = 1.02^{+0.71}_{-0.46}$ Gpc^{-3} yr^{-1} (Ruffini et al. 2016).

Interestingly, it has been shown in Ruffini et al. (2016); Fryer et al. (2015); Becerra et al. (2015) that the *out-states* of long GRBs can become the *in-states* of short GRBs. Since $\rho_{\rm XRF} > \rho_{\rm S-GRF}$ and $\rho_{\rm XRF} > \rho_{\rm S-GRB}$, the *out-states* of XRFs (νNS-NS) could be the *in-states* of S-GRFs (NS-NS mergers leading to a MNS) and S-GRBs (NS-NS mergers leading to a BH).

There is also an additional evolutionary scenario concerning the NS-WD merger, namely that they are produced from an S-GRF (Ruffini et al. 2016). The merger of a mass-asymmetric NS-NS binary with total mass $m_1 + m_2$ smaller than $M_{\rm crit}$ can produce a MNS with a low-mass WD companion (see Bildsten & Cutler 1992, and references therein), a type of binary of great current interest (see, e.g., Lazarus et al. 2014; Tauris et al. 2000).

The rate of occurrence of the above GRB sub-classes has been recently estimated in Ruffini et al. (2016) assuming the absence of beaming. We show in Table 1 a summary of the astrophysical aspects related to the GRB sub-classes and their observational properties. With this knowledge of the compact object binary progenitors associated with each GRB sub-class and their corresponding rate of occurrence, we can now proceed to estimate their GW emission in order to evaluate its possible detectability by aLIGO and bar detectors.

2. GW EMISSION AND DETECTABILITY

In the introduction we have recalled that the evolution of the binary progenitors of both short and long GRBs lead to compact binaries which will eventually merge in a characteristic timescale and emit GWs. We turn now to assess the detectability of the GW emission by these merging binaries by aLIGO.

In order to do this, we make the following drastic gedanken assumptions:

1. Although it is manifest that the release of gravitational energy of the system in the merger phase is dominated by the X, gamma-ray and GeV emission (see Table 1), we assume in Sec. 2.2 that the binary dynamics is only driven by the GW emission.

2. Consistent with the above GW emission dominance assumption, we further assume that the GW waveform is known and thus one can use the matched filter technique to estimate the signal-to-noise ratio (see Sec. 2.1). The actual GW waveform under the realistic conditions of electromagnetic emission dominance is still unknown.

3. To estimate the maximum distance of GW detectability we adopt in Sec. 3 that the source is optimally oriented with respect to the detector.

The above assumptions are made with the only aim of establishing an absolute upper limit to the GW emission and its putative detectability under the most optimistic conditions. Similarly, we assume that the binarity of the system does not compromise the structure of the NS (see Sec. 2.3).

The minimum GW frequency detectable by the broadband aLIGO interferometer is $f_{\rm min}^{\rm aLIGO} \approx 10$ Hz (LIGO Scientific Collaboration et al. 2015). Since during the binary inspiral the GW frequency is twice the orbital one (see below Sec. 2.2), the above implies a binary is inside the aLIGO band for orbital periods $P_{\rm orb} \lesssim 0.2$ s. Thus, we can conclude that $\rm CO_{core}$-NS binaries, *in-states* of XRFs and BdHNe, and $\rm CO_{core}$-BH binaries, *in-states* of BH-SN, are not detectable by aLIGO since they have orbital periods $P_{\rm orb} \gtrsim 5$ min $\gg 0.2$ s. Concerning their *out-states* after the corresponding hypercritical accretion processes, namely νNS-NS, *out-states* of XRFs, and νNS-BH, *out-states* of BdHNe and BH-SNe, they are not detectable by aLIGO at their birth but only when approaching the merger. In the case of NS-WD binaries, the WD large radius and its very likely tidal disruption by the NS make their GW emission hard to be detected (see, e.g., Paschalidis et al. 2009). Thus, we do not consider NS-WD binaries in the following discussion.

It is clear that the analysis of GW emission during the final coalescence and merger of the νNS-NS binaries produced by XRFs is included in the analysis of the S-GRF and S-GRB sub-classes, and the merger of νNS-BH binaries produced in BdHNe and BH-SNe is included in the one of U-GRBs.

In order to define the possible masses of the components of the binary systems, we need information on the NS structure. In particular, we have to establish the maximum stable NS mass, i.e., the critical mass for gravitational collapse to a BH. The critical mass lies within the range 2.2–3.4 $M_\odot$ depending on the equation of state (EOS) and on the NS angular momentum (see Cipolletta et al. 2015; Becerra et al. 2015; Belvedere et al. 2014 for details). These quoted values are for EOS based on relativistic nuclear mean-field models (in this case the NL3, TM1 and GM1 models) and for a NS angular momentum from $J = 0$ up to $J_{\rm max} \approx 0.7GM^2/c$ (Cipolletta et al. 2015). Hereafter, we adopt the stiffest model, namely the NL3 EOS, which leads to the largest NS critical mass: from $M_{\rm crit} \approx 2.7\ M_\odot$ at $J = 0$, that, as expected, is lower than the non-rotating critical mass upper limit of 3.2 $M_\odot$ established by Rhoades & Ruffini (1974), to $M_{\rm crit} \approx 3.4\ M_\odot$ at $J_{\rm max}$ (Cipolletta et al. 2015).

For S-GRFs, we consider the simple case of symmetric binary (NS-NS) mergers, $m_1 = m_2 = m$. The precise value of the merging NS masses leading to a BH is still poorly known, thus we have chosen it as roughly half the maximum NS critical mass. Thus, for the sake of completeness we explore mass values from $m \approx 1\ M_\odot$ to $m \approx 1.7\ M_\odot$.

For S-GRBs, we also consider non-spinning symmetric binary components with values starting from the upper edge of the S-GRF progenitors, i.e. $m \approx 1.7\ M_\odot$, up to the maximum non-rotating stable mass, i.e. $m \approx 2.8\ M_\odot$.

For the U-GRBs which are *out-states* of BdHN we adopt $m_1 = 1.5\ M_\odot$ for the νNS mass and $m_{\rm BH} = 2.7$–$3.4\ M_\odot$ for the BH mass. For the U-GRBs which are *out-states* of BH-SN we adopt $m_1 = 1.5\ M_\odot$ for the νNS mass and $m_{\rm BH} = 3.4$–$10\ M_\odot$ for the BH mass.

2.1. *Signal-to-noise ratio*

We first recall the main ingredients needed to estimate the detectability of the aforementioned merging binaries associated with the different GRB classes. The signal $h(t)$ induced in the detector is:

$$h(t) = F_+(\theta,\phi,\psi)h_+(t,\iota,\beta) + F_\times(\theta,\phi,\psi)h_\times(t,\iota,\beta), \quad (1)$$

where h_+ and $h_\times$ are the two polarizations of the GW; ι and β are the polar and azimuthal angles of the unit vector from the source to the detector, relative to a coordinate system centered in the source. The detector pattern functions F_+ and $F_\times$ depend on the localization of the source with respect to the detector, i.e. they depend on the spherical polar angles θ and ϕ of the source

relative to a coordinate system centered in the detector. The pattern functions also depend on the polarization angle ψ.

Since the GW signal might be deep inside the noise, the signal-to-noise ratio, denoted hereafter by ρ, is usually computed using the matched filter technique, i.e. (Flanagan & Hughes 1998):

$$\rho^2 = 4\int_0^\infty \frac{\left|\tilde{h}(f)\right|^2}{S_n(f)}df, \tag{2}$$

where f is the GW frequency in the detector's frame, $\tilde{h}(f)$ is the Fourier transform of $h(t)$ and $\sqrt{S_n(f)}$ is the one-sided amplitude spectral density (ASD) of the aLIGO noise. We recall that in the detector's frame the GW frequency is redshifted by a factor $1+z$ with respect to the one in the source's frame, f_s, i.e. $f = f_s/(1+z)$.

The exact position of the binary relative to the detector and the orientation of the binary rotation plane are usually unknown, thus it is a common practice to estimate the signal-to-noise ratio averaging over all the possible locations and orientations, i.e.:

$$\langle\rho^2\rangle = 4\int_0^\infty \frac{\langle|\tilde{h}(f)|^2\rangle}{S_n(f)}df = 4\int_0^\infty \frac{h_c^2(f)}{f^2 S_n(f)}df, \tag{3}$$

with $h_c(f)$ the characteristic strain (Flanagan & Hughes 1998)

$$h_c = \frac{(1+z)}{\pi d_l}\sqrt{\frac{\langle F_+^2\rangle}{2}\frac{G}{c^3}\frac{dE}{df_s}[(1+z)f]}, \tag{4}$$

where

$$d_l = \frac{(1+z)c}{H_0}\int_0^z [\Omega_M(1+x)^3+\Omega_\Lambda]^{-1/2}dx, \tag{5}$$

is the source luminosity distance and we have used the fact that $\langle F_+^2\rangle = \langle F_\times^2\rangle$ and $\langle F_+ F_\times\rangle = 0$. We recall that $\langle F_+^2\rangle = 1/5$ for an interferometer and $\langle F_+^2\rangle = 4/15$ for a resonant bar (see, e.g., Maggiore 2007). We adopt a ΛCDM cosmology with $H_0 = 71$ km s^{-1} Mpc^{-1}, $\Omega_M = 0.27$ and $\Omega_\Lambda = 0.73$ (Rigault et al. 2015). It is important to recall that, as we have mentioned, we are interested in estimating the GW detectability under the most optimistic conditions. Thus, to estimate the maximum distance of GW detectability we adopt in Sec. 3 the ansatz of optimally oriented sources with respect to the detector. The above averaging procedure is here used with the only aim of giving an estimate of the GW strain amplitude, h_c, compared and contrasted below in Sec. 2.4 with the strain noise of the detectors.

2.2. *GW energy spectrum*

A binary system, by emitting GWs, evolves in time through two regimes: the first is the *inspiral regime* and the second, which we refer hereafter to as *merger regime*, is composed in the most general case of the final plunge, of the merger, and of the ringdown (oscillations) of the newly formed object.

During the inspiral regime the system evolves describing quasi-circular orbits and it is well described by the traditional point-like quadrupole approximation (Peters & Mathews 1963; Peters 1964; Rees et al. 1974; Landau & Lifshitz 1975). The GW frequency is twice the orbital frequency ($f_s = 2f_{\rm orb}$) and grows monotonically. The energy spectrum during the inspiral regime is:

$$\frac{dE}{df_s} = \frac{1}{3}(\pi G)^{2/3}M_c^{5/3}f_s^{-1/3}, \tag{6}$$

where $M_c = \mu^{3/5}M^{2/5} = \nu^{3/5}M$ is the called *chirp mass*, $M = m_1 + m_2$ is the total binary mass, $\mu = m_1 m_2/M$ is the reduced mass, and $\nu \equiv \mu/M$ is the symmetric mass-ratio parameter. A symmetric binary ($m_1 = m_2$) corresponds to $\nu = 1/4$ and the test-particle limit is $\nu \to 0$. The total energy emitted during this regime can be estimated as the binding energy of the binary at the last stable circular orbit (LSO). For a test-particle in the Schwarzschild background, the LSO is located at $r_{\rm LSO} = 6GM/c^2$ and the binding energy is:

$$\Delta E_{\rm insp} = \left(1 - 2\sqrt{2}/3\right)\mu c^2. \tag{7}$$

The GW spectrum of the merger regime is characterized by a GW burst (see, e.g., Davis et al. 1971; Shibata & Taniguchi 2011; Bernuzzi et al. 2015a). Thus, to estimate whether this part of the signal contributes to the signal-to-noise ratio, it is sufficient to estimate the location of the GW burst in the frequency domain and its energy content. We recall that, in general, the merger regime is composed of plunge+merger+ringdown. The frequency range spanned by the GW burst is $\Delta f = f_{\rm qnm} - f_{\rm merger}$, where $f_{\rm merger}$ is the frequency at which the merger starts and $f_{\rm qnm}$ is the frequency of the ringing modes of the newly formed object after the merger, and the energy emitted is $\Delta E_{\rm merger}$. With these quantities defined, we can estimate the typical value of the merger regime spectrum as:

$$\left(\frac{dE}{df_s}\right)_{\rm merger} \sim \frac{\Delta E_{\rm merger}}{\Delta f}. \tag{8}$$

2.3. *GW energy and frequency in the merger regime*

2.3.1. *NS-NS merger*

Numerical relativity simulations (e.g. Shibata & Taniguchi 2011; Bernuzzi et al. 2015a) show that finite size effects might end the inspiral regime before the LSO. After this point, the GW spectrum damps exponentially. For the case of NS-NS the merger starts in an orbit larger than the LSO, and for the case of a NS-BH, as we will see below, the merger can occur below the LSO making the spectrum similar to a BH-BH merger. When the merger occurs well before the LSO, there is not the plunge. Therefore, the emitted energy will be less than the case when the plunge is present. We can therefore obtain an upper limit to $\Delta E_{\rm merger}$ by adopting the energy emitted during the plunge-merger-ringdown of a BH-BH merger (Detweiler & Szedenits 1979; Nagar et al. 2007)

$$\Delta E_{\rm merger} \approx 0.5\nu^2 Mc^2. \tag{9}$$

To complete the estimate of the merger regime spectrum, we have to estimate the value of Δf in the different cases of interest. The approach to the merger point, $r = r_{\rm merger}$, depends on the nature of the binary system. Typically, the merger is assumed to start at the point of maximum GW strain (see, e.g., Bernuzzi et al.

Table 2
Properties of the GW emission of S-GRFs, S-GRBs and U-GRBs. We have made the drastic gedanken assumption that the binary evolution is only driven by GW emission, although it is manifest that the gravitational energy of the system in the merger phase is dominated by the radio, optical, X, gamma-ray and GeV emission (see Table 1). This assumption is made with the only aim of establishing an absolute upper limit to the GW emission and its detectability under the most optimistic conditions. Column 1: GRB sub-class. Column 2: energy emitted in GWs during the inspiral regime $\Delta E_{\rm insp}$ given by Eq. (7). Column 3: energy emitted in GWs during the merger regime (plunge+merger+ringdown) $\Delta E_{\rm merger}$ given by Eq. (9). Columns 4: GW frequency at merger. Column 5: GW frequency of the ringdown regime. Column 6: lowest cosmological redshift value $z^{\rm obs}_{\rm min}$ at which each sub-class has been observed. Column 7: luminosity distance corresponding to $z^{\rm obs}_{\rm min}$, $d_{l_{\rm min}}$, estimated from Eq. (5). Columns 8 and 9: GW horizon calculated with the sensitivity of the first run of aLIGO (O1) and the expected final sensitivity (2022+), respectively. It can be seen that the current GW horizon is much smaller than the observed distances of GRBs, impeding a positive detection by aLIGO. Only in the case of U-GRB (BH-SN) it is foreseen a possible detection during the run 2022+. See also Table 3. We have used for S-GRFs (1.4+1.4) $M_\odot$, for S-GRBs (2.0+2.0) $M_\odot$ and, for U-GRBs (1.5+3.0) $M_\odot$ and (1.5+10.0) $M_\odot$ respectively for the *out-states* of BdHNe and of BH-SN. Even if no U-GRB has yet been identified, we use here the values of $z^{\rm obs}_{\rm min}$ and $d_{l_{\rm min}}$ corresponding to the closest BdHN observed.

	$\Delta E_{\rm insp}$ (erg)	$\Delta E_{\rm merger}$ (erg)	$f_{\rm merger}$ (kHz)	$f_{\rm qnm}$ (kHz)	$z^{\rm obs}_{\rm min}$	$d_{l_{\rm min}}$ (Mpc)	$d_{\rm GW}$ (Mpc) O1	2022+
S-GRF	7.17×10^{52}	1.60×10^{53}	1.20	3.84	0.111	508.70	168.43	475.67
S-GRB	1.02×10^{53}	2.28×10^{53}	1.43	2.59	0.903	5841.80	226.62	640.18
U-GRB	1.02×10^{53}	2.03×10^{52}	0.98	2.30	0.169	804.57	235.62	665.72
U-GRB (BH-SN)	1.34×10^{53}	1.35×10^{53}	0.38	0.90	0.169	804.57	362.27	1023.43

2015a, and references therein). However, since the transition from a binary system to a single merged object is not sharply definable, there can be found different definitions of the merger point in the literature (see, e.g., Kawaguchi et al. 2015). For our purpose it is sufficient to estimate the frequency at "contact", namely the frequency at a binary separation $r_{\rm contact}\approx r_1+r_2$ where r_i is the radius of the i-component. This certainly sets a lower limit to the frequency at maximum strain at merger, i.e. $r_{\rm contact}\gtrsim r_{\rm merger}$. Thus, we adopt for these systems:

$$f^{\rm NS-NS}_{\rm merger}\approx f^{\rm NS-NS}_{\rm contact}=\frac{1}{\pi}\frac{c^3}{GM}\left[\frac{\mathcal{C}_1\mathcal{C}_2(1+q)}{\mathcal{C}_1+q\mathcal{C}_2}\right]^{3/2}, \quad (10)$$

where $q=m_2/m_1$ is the mass-ratio which is related to the symmetric mass-ratio parameter by $\nu=q/(1+q)^2$, and $\mathcal{C}_i\equiv Gm_i/c^2r_i$ is the compactness of the i-component.

For a mass symmetric NS-NS binary, we have that $f^{\rm NS-NS}_{\rm contact}\approx(1/\pi)(c^3/G)\mathcal{C}^{3/2}_{\rm NS}/M$, where $\mathcal{C}_{\rm NS}\equiv\mathcal{C}_1=\mathcal{C}_2$ is the compactness parameter of the initial NS. For example, for the NL3 EOS, the NS compactness lies in the range $\mathcal{C}_{\rm NS}\approx 0.14$–$0.3$ for a NS mass 1.4–2.8 $M_\odot$ (see, e.g., Cipolletta et al. 2015). Thus, using the same EOS we have, for an $M=(1.4+1.4)\ M_\odot=2.8\ M_\odot$ binary, $f^{\rm NS-NS}_{\rm contact}\approx 1.34$ kHz, and for an $M=(2.0+2.0)\ M_\odot=4.0\ M_\odot$ binary, $f^{\rm NS-NS}_{\rm contact}\approx 1.43$ kHz.

In the merger regime either a BH or a MNS can be formed. If a BH is formed, the $l=2$ multipole (quadrupole) quasi-normal oscillations lead to a spectrum that peaks at a frequency (Davis et al. 1971, 1972)

$$f^{\rm BH}_{\rm qnm}\approx\frac{0.32}{2\pi}\frac{c^3}{GM}, \quad (11)$$

i.e. $f_{\rm qnm}\approx 3.4$ kHz for a Schwarzschild BH of 3 $M_\odot$. In the case of a rotating BH, namely a Kerr BH, the peak frequency shifts to higher values (Detweiler 1980). Thus, the value of $f^{\rm BH}_{\rm qnm}$ for a non-rotating BH can be considered as a lower bound to the peak frequency.

When the merger does not lead to a BH, the merger frequency is dominated by the oscillations of a MNS. This last frequency is of the order of

$$f^{\rm MNS}_{\rm qnm}\approx\frac{1}{\pi}\left(\frac{GM}{R^3}\right)^{1/2}=\frac{1}{\pi}\left(\frac{c^3}{G}\right)\frac{\mathcal{C}^{3/2}_{\rm MNS}}{M}, \quad (12)$$

where R is the radius of the MNS and $\mathcal{C}_{\rm MNS}\equiv GM/(c^2R)$ is its compactness. In either case of BH or MNS formation, it is satisfied $f_{\rm qnm}>f_{\rm contact}$. It can be checked that the above frequency estimates are consistent with values obtained from full numerical relativity simulations (see, e.g., Rodriguez et al. 2016; Anninos et al. 1995; Bernuzzi et al. 2015a).

2.3.2. *NS-BH merger*

For a NS-BH merger, the approach to merger is different since general relativistic effects avoid the objects to go all the way to the "contact" point following circular orbits. For example, let us assume $m_1=m_{\rm BH}\approx 3\ M_\odot$ and $m_2=M_{\rm NS}\approx 1.5\ M_\odot$, so $M=1.5+3.0\ M_\odot=4.5\ M_\odot$. In this case $r_1=2Gm_{\rm BH}/c^2$ (for a Schwarzschild BH) and $r_2=Gm_2/(c^2\mathcal{C}_2)$, so $r_{\rm contact}\approx 3.3GM/c^2$. Within the test-particle limit, the LSO around a Schwarzschild BH occurs at $r_{\rm LSO}=6Gm_{\rm BH}/c^2\approx 6GM/c^2>r_{\rm contact}$. Taking into account finite-mass and tidal effects does not change this conclusion (on the contrary, the LSO becomes bigger; see Bernuzzi et al. 2015b). Thus, we have that $r_{\rm contact}<r_{\rm LSO}$ which suggests that a NS-BH binary, similar to the case of a BH-BH one, can pass from the inspiral regime, to the plunge from $r_{\rm plunge}=r_{\rm LSO}$ to merger at $r_{\rm merger}\approx r_{\rm contact}$, to the ringing of the newly formed BH. At $r_{\rm plunge}$, the GW frequency is

$$f^{\rm NS-BH}_{\rm plunge}\approx\frac{1}{\pi}\left(\frac{GM}{r^3_{\rm LSO}}\right)^{1/2}=\frac{1}{\pi 6^{3/2}}\left(\frac{c^3}{GM}\right), \quad (13)$$

and as in the previous case of BH formation from a NS-NS merger, the NS-BH post-merger GW spectrum will be dominated by frequencies given by Eq. (11). Namely, for the present example $f^{\rm NS-BH}_{\rm plunge}\approx 980$ Hz and $f^{\rm BH}_{\rm qnm}\approx 2.3$ kHz.

In the above analysis we have neglected the possibility that the NS can be tidally disrupted by the BH before it reaches $r=r_{\rm LSO}$. The NS is disrupted by the

BH if $r_{\rm LSO} < r_{\rm td}$, where $r_{\rm td}$ is the tidal disruption radius. Numerical simulations of NS-BH binary mergers suggest $r_{\rm td} \lesssim 0.45 q^{-1/3} R_{\rm NS}$ (see Shibata & Taniguchi 2011, and references therein), where $q \equiv m_2/m_1 \leq 1$ is the binary mass-ratio. To evaluate whether $r_{\rm LSO} < r_{\rm td}$ or $r_{\rm LSO} > r_{\rm td}$, we need to compute the LSO accounting for tidal effects on the NS, since they make the effective potential more attractive with respect to the point-like one (Bernuzzi et al. 2015b). From simulations of NS-BH binaries (with $m_{\rm BH} = 3\ M_\odot$ and for $q \leq 1$) via the effective one-body formalism at 4th post-Newtonian order including the tidal potential, we have obtained $r_{\rm LSO} \approx 5(GM/c^2)q^{2/5}$ (Gizzi & Rueda 2016). This implies tidal disruption for values of the NS compactness $\mathcal{C}_{\rm NS} < \mathcal{C}_{\rm NS,td} = 0.09 q^{4/15}/(1+q)$. For $1.5+3.0\ M_\odot$ and $1.5+10.0\ M_\odot$ νNS-BH binaries, we have $\mathcal{C}_{\rm NS} \approx 0.15$ and $\mathcal{C}_{\rm NS,td} \approx 0.05$, thus tidal disruption of the NS by the BH seems to be unlikely in both cases, as we have supposed.

2.4. *Characteristic strain and detectors sensitivity*

From Eqs. (6) and (8) and with the knowledge of the energy released in GWs (9) and the spanned frequencies in the merger regime (see Table 2), we can estimate the characteristic strain (4) which can be compared and contrasted with the strain noise of GW detectors.

Fig. 1 shows the GW signal ASD produced by S-GRFs, S-GRBs and U-GRBs, obtained with the aid of Eq. (4). In this figure we adopt: a $(1.4+1.4)\ M_\odot$ νNS-NS merger for S-GRFs, a $(2.0+2.0)\ M_\odot$ νNS-NS merger for S-GRBs, a $(1.5+3.0)\ M_\odot$ νNS-BH merger for U-GRBs produced by *out-states* of BdHNe, and a $(1.5+10.0)\ M_\odot$ νNS-BH merger for U-GRBs produced by *out-states* of BH-SNe. We have assumed in this plot that these sources are located at the closest luminosity distance d_l at which each sub-class has been observed (see Table 2 for details). We show the noise ASD of aLIGO in the current run (O1) and in the expected 2022+ run (Abbott et al. 2016); the expected noise ASD of AdV (BNS-optimized; Abbott et al. 2016); the expected noise ASD of the space-based interferometer eLISA for the N2A1, N2A2 and N2A5 configurations (see, e.g., Klein et al. 2016); and the noise ASD of the NAUTILUS bar detector for a 1 ms GW burst (Astone et al. 2006, 2008). Narrow-band resonant bar detectors (such as ALLEGRO, AURIGA, EXPLORER, NAUTILUS and NIOBE) are sensitive within a bandwidth of $\sim$ 1–10 Hz around the resonant frequency which is typically $f_0 \sim 1$ kHz (see, e.g., Table 2 in Camp & Cornish 2004, for a summary of the properties of the bar detectors). The bar detector with the wider bandwidth is NAUTILUS with a minimum strain spectral noise $\sqrt{S_n} = 10^{-21}$ Hz$^{-1/2}$ at $f_0 = 935$ Hz and $\sqrt{S_n} \leq 10^{-20}$ Hz$^{-1/2}$ in a bandwidth ~ 30 Hz around f_0 (Astone et al. 2008). This implies that a 1 ms GW burst would be detected by this instrument if it has a strain amplitude $h \gtrsim 3 \times 10^{-19}$ (Astone et al. 2006, 2008).

From this figure we can conclude for the NS-NS and NS-BH binaries associated with S-GRFs, S-GRBs and U-GRBs:

1. *Before merging:* they transit, during their inspiral regime which spans the frequency range $f < f_{\rm merger}/(1+z)$ (see in Table 2 the frequencies and redshift), first the eLISA frequency band to then enter the aLIGO and AdV ones in the final orbits prior the merging process (when $P_{\rm orb} < 0.2$ s). The narrow bandwidth of the bar detectors does not cover these frequencies. For the adopted distances we see that the characteristic strain generated by all these sources is below the sensitivity of eLISA. S-GRFs are below the sensitivity of aLIGO (O1), AdV and NAUTILUS, but inside the sensitivity of aLIGO (2022+). S-GRBs are below the sensitivity of aLIGO (all runs), AdV and NAUTILUS. U-GRBs from *out-states* of BdHNe are below the sensitivity of aLIGO (O1), AdV and NAUTILUS, but inside the sensitivity of aLIGO (2022+). U-GRBs from *out-states* of BH-SNe are below the sensitivity of aLIGO (O1) and NAUTILUS, inside the sensitivity of aLIGO (2022+), and marginally inside the sensitivity of AdV.

2. *Merging:* the merging regime, which expands frequencies from $f_{\rm contact}/(1+z)$ to $f_{\rm qnm}/(1+z)$ (see in Table 2 the frequencies and redshift), is outside the eLISA frequency band but inside the aLIGO, AdV and bar detectors ones. The characteristic strain in this final merger phase $h \sim 10^{-24}$–10^{-23} is, unfortunately, well below the sensitivity of all of them (see also Kobayashi & Mészáros 2003 for similar conclusions for aLIGO).

From the above it can be seen that the most interesting instrument for the possible detection of the GW emission from binaries associated with GRBs is aLIGO. Therefore, we estimate in the next section the expected detection rates by aLIGO (see Fig. 2 and Table 3).

3. GW DETECTION RATE

We assume a threshold for the aLIGO single detector $\rho_0 = 8$ (Abbott et al. 2016). This minimum ρ_0 defines a maximum detection distance or GW horizon distance, which is denoted as $d_{\rm GW}$. This horizon corresponds to the most optimistic case when the binary is just above the detector and the binary plane is parallel to the detector plane, i.e. $\theta = \phi = \iota = 0$ (Allen et al. 2012):

$$d_{\rm GW} = \frac{2A}{\rho_0}\left(\int_0^\infty \frac{f^{-7/3}}{S_n(f)}df\right)^{1/2}, \qquad (14)$$

where $A = 5/(24\pi^{4/3})^{1/2}(GM_c/c^3)^{5/6}c$. We show in Table 2 GW horizon for S-GRFs, S-GRBs and U-GRBs. Since not all the sources are optimally aligned with the detector, the number of detected sources inside a sphere of radius $d_{\rm GW}$ will be a fraction $\mathcal{F}^3$ of the total. This fraction determines the range of the detector $\mathcal{R} = \mathcal{F} d_{\rm GW}$, with $\mathcal{F}^{-1} = 2.2627$ (Finn & Chernoff 1993). In order to give an estimate of the annual number of detectable binaries associated with GRBs we use the *search volume* as computed in (Abbott et al. 2016), $\mathcal{V}_s = V_{\rm max}^{\rm GW}\mathcal{T}$, where $V_{\rm max}^{\rm GW} = (4\pi/3)\mathcal{R}^3$ and $\mathcal{T}$ is the observing time. We use here the lower and upper values of $\mathcal{V}_s$ for a (1.4+1.4) $M_\odot$ NS binary for the different observational campaigns reported in (Abbott et al. 2016): 2015/2016 (O1) with $\mathcal{T} = 3$ months, $\mathcal{V}_S = (0.5$–$4) \times 10^5$ Mpc^3 yr, 2017/2018 (O3) with $\mathcal{T} = 9$ months, $\mathcal{V}_S = (3$–$10) \times 10^6$ Mpc^3 yr, and the one by the entire network including LIGO-India at design sensitivity (2022+) with $\mathcal{T} = 1$ yr, $\mathcal{V}_S = 2 \times 10^7$ Mpc^3 yr. The

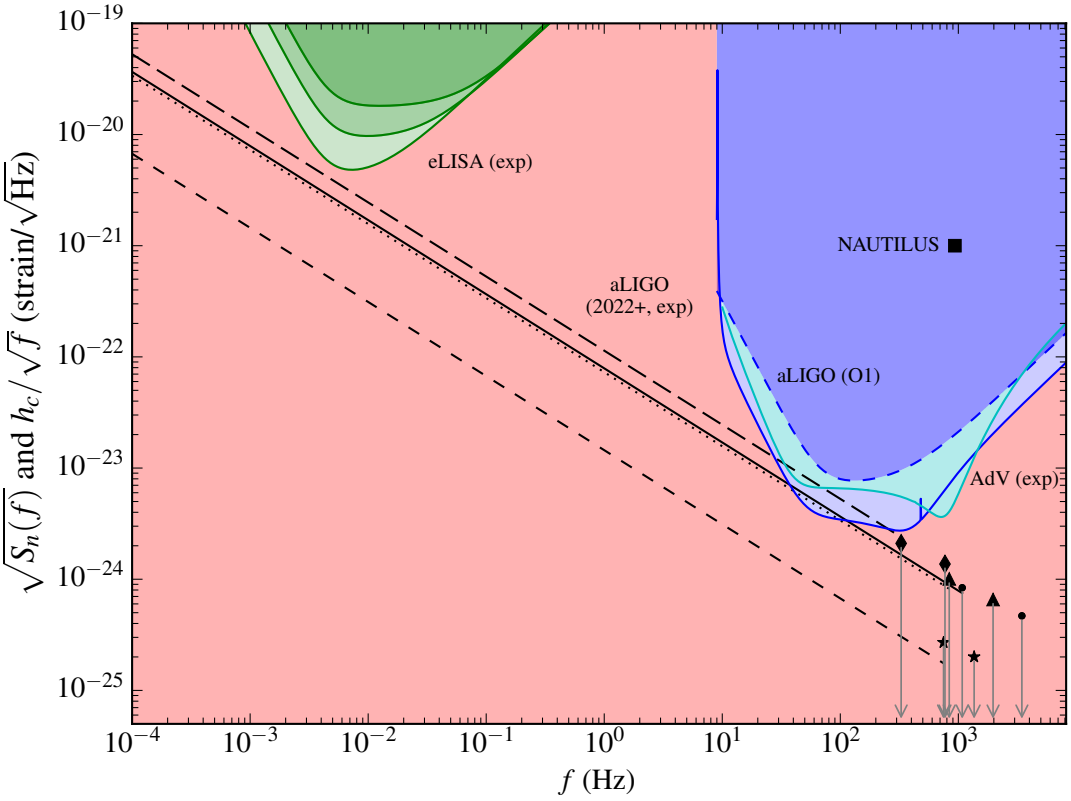

Figure 1. Comparison of the signal's ASD $h_c/\sqrt{f}$ of S-GRFs, S-GRBs and U-GRBs with the noise's ASD $\sqrt{S_n(f)}$, where S_n is the power spectrum density of the detector's noise of eLISA, of aLIGO and of the bar detector NAUTILUS. The green lines, from top to bottom, are the expected noise's ASD of the N2A1, N2A2 and N2A5 configurations of eLISA (Klein et al. 2016). The dashed and continuous blue lines correspond to the noise's ASD respectively of aLIGO O1 run (2015/2016) and of the expected aLIGO 2022+ run (Abbott et al. 2016), and the cyan line is the expected noise's ASD of AdV (BNS-optimized; Abbott et al. 2016). The filled square indicates the noise's ASD of the NAUTILUS resonant bar for a 1 ms GW burst (Astone et al. 2006, 2008). The red filled area indicates the region of undetectability by any of the above instruments. We recall that in this plot the GW frequency is redshifted by a factor $1+z$ with respect to the source frame value, i.e. $f = f_s/(1+z)$, for which we use the cosmological redshift and corresponding luminosity distance of the closest observed source of each sub-class (see Table 2). The following three curves correspond to the inspiral regime of the coalescence: S-GRFs with $(1.4+1.4)\ M_\odot$ (solid curve), S-GRBs with $(2.0+2.0)\ M_\odot$ (short-dashed curve), U-GRB with $(1.5+3.0)\ M_\odot$ (dotted curve) from *out-states* of BdHNe, and U-GRB with $(1.5+10.0)\ M_\odot$ (long dashed curve) from *out-states* of BH-SNe. The dot, star, triangle and diamond correspond to h_c in the merger regime for S-GRFs, S-GRBs, U-GRBs from *out-states* of BdHNe, and U-GRBs from *out-states* of BH-SNe, respectively. The first point is located at $f_{\rm merger}/(1+z)$ and the second at $f_{\rm qnm}/(1+z)$ (see Table 2). The down-arrows indicate that these estimates have to be considered as upper limits since we have assumed that all the energy release in the system goes in GWs, which clearly overestimates the GW energy output in view of the dominance of the electromagnetic emission (see Table 3). We have also overestimated the GW energy in the merger regime by using Eq. (9) which is the expected GW energy emitted in the plunge+merger+ringdown phases of a BH-BH merger. For binary mergers involving NSs, as we have discussed in Sec. 2.3, the energy released in GWs must be necessarily lower than this value.

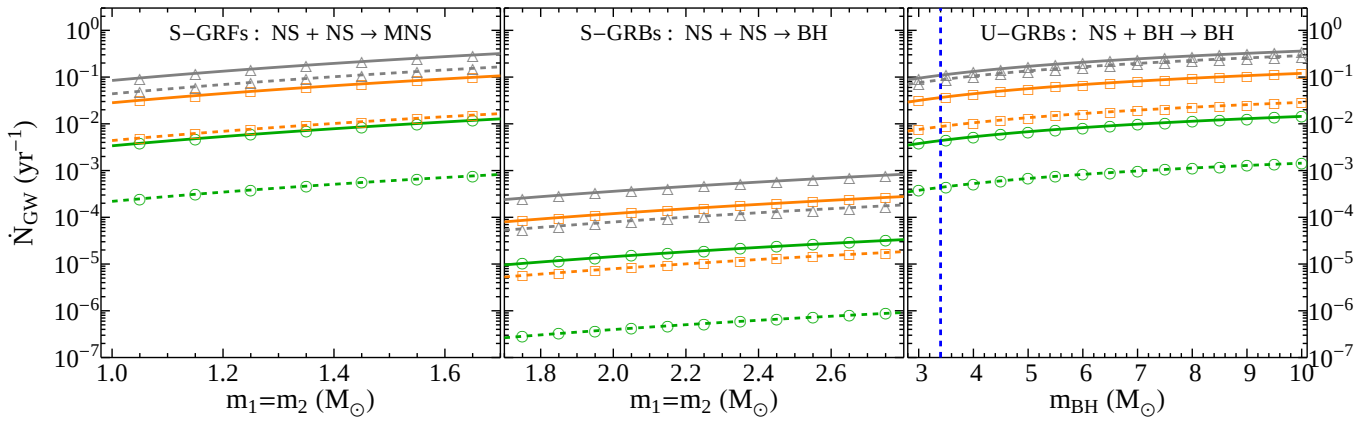

Figure 2. Expected annual GW upper and lower bounds (the solid and the dashed lines, respectively) for the detections expected from S-GRFs (left panel), S-GRBs (middle panel), and U-GRBs (right panel), for three selected observational campaigns: 2015/2016 (O1: green curves with circles), 2017/2018 (O3: orange curve with squares), and 2022+ (gray curve with triangles). The vertical blue dashed line in the plot of U-GRBs separates νNS-BH binaries produced by BdHN (BH masses equal to the NS critical mass) and BH-SN (BH masses larger than the NS critical mass).

Table 3

Column 1: GRB sub-class. Column 2: inferred number of GRBs per year in the entire Universe, $\dot{N}_{\rm GRB}$, for each GRB sub-class (see also Fig. 6 in Ruffini et al. 2016). Column 3: number of GRBs observed per year, $\dot{N}^{\rm obs}_{\rm GRB}$, obtained from the observations of γ-ray telescopes such as AGILE, BATSE, BeppoSAX, *Fermi*, *HETE-II*, *INTEGRAL*, Konus/WIND and *Swift*, in the indicated years of observations (see also Tables 2–6 in Ruffini et al. 2016). Column 4: expected rate of GW detections by aLIGO of all the GRB sub-classes, computed for three selected observational campaigns: 2015/2016 (O1), 2017/2018 (O3) and the one by the entire network including LIGO-India at design sensitivity, 2022+. The typical masses used here are the same of Table 2.

GRB sub-class	$\dot{N}_{\rm GRB}$ (yr^{-1})	$\dot{N}^{\rm obs}_{\rm GRB}$ (yr^{-1})	$\dot{N}_{\rm GW}$ (yr^{-1})
XRFs	144–733	1 (1997–2014)	undetectable
BdHNe	662–1120	14 (1997–2014)	undetectable
BH-SN	$\lesssim$ 662–1120	$\lesssim$ 14 (1997–2014)	undetectable
S-GRFs	58–248	3 (2005–2014)	O1: $(0.4–8)\times10^{-3}$ O3: 0.011–0.065 2022+: 0.1–0.2
S-GRBs	2–8	1 (2006–2014)	O1: $(0.4–8)\times10^{-6}$ O3: $(0.08–1.2)\times10^{-4}$ 2022+: $(0.8–3.6)\times10^{-4}$
U-GRBs	662–1120	–	O1: $(0.36–3.6)\times10^{-3}$ O3: 0.008–0.032 2022+: 0.076–0.095
U-GRBs (BH-SN)	$\lesssim$ 662–1120	–	O1: 0.0016–0.016 O3: $\lesssim$ 0.029–0.12 2022+: $\lesssim$ 0.3–0.36
GRFs	29-153	1 (2005–2014)	undetectable

maximum possible sensitivity reachable in 2022+ leads to $d_{\rm GW} \approx 0.2$ Gpc, hence $V^{\rm GW}_{\rm max} \approx 0.033$ Gpc^3, for such a binary. We can use this information for a (1.4+1.4) $M_\odot$ binary and extrapolate it to other binaries with different masses since the $d_{\rm GW}$ scales with the chirp mass as $M_c^{5/6}$ (see Fig. 2).

From the inferred occurrence rates $\rho_{\rm GRB}$ (not to be confused with signal-to-noise ratio ρ) summarized in Table 1, we show in Fig. 2 the expected number of GW detections by aLIGO

$$\dot{N}_{\rm GW} = \rho_{\rm GRB} V^{\rm GW}_{\rm max}, \tag{15}$$

for S-GRFs, S-GRBs, and U-GRBs.

We compare and contrast in Table 3 for the GRB sub-classes: the expected GW detection rate by aLIGO given by Eq. (15), $\dot{N}_{\rm GW}$, the inferred occurrence rate of GRBs, $\dot{N}_{\rm GRB}$, and the observed GRB rate from γ-ray telescopes (AGILE, BATSE, BeppoSAX, *Fermi*, *HETE-II*, *INTEGRAL*, Konus/WIND and *Swift*), simply estimated as $\dot{N}^{\rm obs}_{\rm GRB} = N^{\rm obs}_{\rm GRB}/T_{\rm obs}$ where $N^{\rm obs}_{\rm GRB}$ is the number of GRBs detected in the observing time $T_{\rm obs}$. The rate $\dot{N}_{\rm GRB}$ is obtained from the GRB specific rate through the reconstruction of the GRB luminosity function and the study of its evolution with the redshift (see Ruffini et al. 2016, for details). This estimate, therefore, is larger than $\dot{N}^{\rm obs}_{\rm GRB}$ which is limited to those events beyond the detector sensitivity threshold, falling inside its field of view and within its operational time.

4. CONCLUSIONS

Short and long GRBs have been divided into 7 sub-classes according to their binary nature (Ruffini et al. 2016). We summarize in Table 1 their main physical properties characterizing the outcome of X-rays, gamma-rays, high-energy and ultra high-energy detectors, as well as their occurrence rate. Particularly important for the present work is the specification of the *in-states* and *out-states* of the GRB progenitors.

With the knowledge of the nature of the compact object binaries associated with each GRB sub-class, we describe in Sec. 2 the general properties of the GW emission during the inspiral and merger regimes of these binaries. We argue that S-GRFs, S-GRBs and U-GRBs are the GRB sub-classes relevant for the GW analysis. It is manifest that the release of the gravitational energy gain of the system in the merger phase is dominated by the X-rays, gamma-rays and GeV emission (see Table 1). In order to evaluate the GW emission we have made in this work the drastic gedanken assumption that the binary evolution is only driven by GW emission. This assumption is of interest with the only aim of establishing an absolute upper limit and to check the detectability of the GW emission under this most optimistic condition. We compare and contrast in Sec. 2.4 the GW characteristic strain amplitude produced by the inspiral and merger regimes with the strain noise of the broadband detectors eLISA, aLIGO and AdV as well as of the narrow-band resonant bar NAUTILUS. In order to do this we use the cosmological redshift and corresponding luminosity distance of the closest observed source of each sub-class (see Table 2). We show that the inspiral regime is possibly detectable only by aLIGO (see Table 2 and Fig. 1) and the merger regime is undetectable by any of these instruments.

Therefore, in Sec. 3 we assess quantitatively the GW detectability of the inspiral regime of S-GRFs, S-GRBs and U-GRBs only by aLIGO. We recall that, following (Abbott et al. 2016), we adopt as the threshold for detectability a signal-to-noise ratio equal to 8. We present in Fig. 2 and Table 3 the expected detection rate of the gedanken GW emission. Three observational campaigns of aLIGO are analyzed: O1 (2015/2016), O3 (2017/2018), and 2022+ namely the one by the entire network including LIGO-India at design sensitivity. In Table 3 we compare and contrast this rate with the occurrence rate of the GRB sub-classes and their rate of observations by γ-ray telescopes.

Keeping the above in mind, we conclude for each GRB sub-class:

I. **XRFs:** their νNS-NS *out-states* transit, during the inspiral regime which spans the frequency range $f < f_{\rm merger}/(1+z)$ (see Table 2), first the eLISA frequency band to then enter the aLIGO and AdV ones in the final orbits prior to the merging process (i.e. when $P_{\rm orb} < 0.2$ s). Resonant bar detectors are not sensitive in this inspiral regime frequency range. The characteristic strain generated by these sources in the inspiral regime is below the sensitivity of eLISA. The merger regime, which expands frequencies from $f_{\rm contact}/(1+z)$ to $f_{\rm qnm}/(1+z)$ (see Table 2), is outside the eLISA frequency band but inside the frequency band of aLIGO, AdV and bar detectors. See Fig. 1 for details. These νNS-NS mergers can lead either to S-GRFs or S-GRBs (see in IV and V below the conclusion about their GW detectability).

II. **BdHNe:** their νNS-BH *out-states* transit, during the inspiral regime which spans the frequency range $f < f_{\rm merger}/(1+z)$ (see Table 2), first the eLISA frequency band to then enter the aLIGO and AdV ones in the final orbits prior to the merging process (i.e. when $P_{\rm orb} < 0.2$ s). Resonant bar detectors are not sensitive in this inspiral regime frequency range. The characteristic strain generated by these sources in the inspiral regime is below the sensitivity of eLISA. The merger regime, which expands frequencies from $f_{\rm contact}/(1+z)$ to $f_{\rm qnm}/(1+z)$ (see Table 2), is outside the eLISA frequency band but inside the frequency band of aLIGO, AdV and bar detectors. See Fig. 1 for details. These νNS-BH mergers lead to U-GRBs (see in VI below the conclusion about their GW detectability).

III. **BH-SN:** their νNS-BH *out-states* transit, during the inspiral regime which spans the frequency range $f < f_{\rm merger}/(1+z)$ (see Table 2), first the eLISA frequency band to then enter the aLIGO and AdV ones in the final orbits prior to the merging process (i.e. when $P_{\rm orb} < 0.2$ s). Resonant bar detectors are not sensitive in this inspiral regime frequency range. The characteristic strain generated by these sources in the inspiral regime is below the sensitivity of eLISA. The merger regime, which expands frequencies from $f_{\rm contact}/(1+z)$ to $f_{\rm qnm}/(1+z)$ (see Table 2), is outside the eLISA frequency band

but inside the frequency band of aLIGO, AdV and bar detectors. See Fig. 1 for details. These νNS-BH mergers lead to U-GRBs (see in VI below the conclusion about their GW detectability).

IV. **S-GRFs:** the final orbits of the inspiral regime (when $P_{\rm orb} < 0.2$ s) fall inside the frequency band of aLIGO, AdV and bar detectors. However, the gedanken GW energy output in the merger regime leads to a characteristic strain which is not sufficient to be detectable either by any of them. See Fig. 1 for details. The inspiral regime is detectable for sources located at distances smaller than 168 Mpc for the O1 aLIGO run and smaller than 476 Mpc for the 2022+ run (see Table 2). The closest S-GRF observed up to now is, however, located at 509 Mpc. See Table 3 for the gedanken GW detection rate.

V. **S-GRBs:** the final orbits of the inspiral regime (when $P_{\rm orb} < 0.2$ s) fall inside the frequency band of aLIGO, AdV and bar detectors. However, the gedanken GW energy output in the merger regime leads to a characteristic strain which is not sufficient to be detectable either by any of them. See Fig. 1 for details. The inspiral regime is detectable for sources located at distances smaller than 227 Mpc for the O1 aLIGO run and smaller than 640 Mpc for the 2022+ run (see Table 2). The closest S-GRB observed up to now is, however, located at 5842 Mpc. See Table 3 for the gedanken GW detection rate.

VI. **U-GRBs:** the final orbits of the inspiral regime (when $P_{\rm orb} < 0.2$ s) fall inside the frequency band of aLIGO, AdV and bar detectors. However, the gedanken GW energy output in the merger regime leads to a characteristic strain which is not sufficient to be detectable either by any of them. See Fig. 1 for details. In the case of U-GRBs originating from the BdHN *out-states*, the inspiral regime is detectable for sources located at distances smaller than 235 Mpc for the O1 aLIGO run and smaller than 666 Mpc for the 2022+ run (see Table 2). In the case of U-GRBs originating from the BH-SN *out-states*, the inspiral regime is detectable for sources at distances smaller than 362 Mpc for the O1 aLIGO run and smaller than 1023 Mpc for the 2022+ run (see Table 2). No U-GRB has yet been electromagnetically identified. The closest distance at which is located its possible progenitor, namely a BdHN, is 805 Mpc. See Table 3 for the gedanken GW detection rate.

VII. **GRFs:** The tidal disruption of the WD by the NS produces a not detectable GW emission (see, e.g., Paschalidis et al. 2009).

The most favorable case for the gedanken GW detection by aLIGO, with a rate of $\dot{N}_{\rm GW} = 0.1$–0.2 yr^{-1}, is that of S-GRFs (see Table 3). In such systems however no BH is formed. The merger of the two NSs will instead lead to a MNS. Among those producing a BH, the most favorable cases are that of U-GRBs from BdHNe with a gedanken rate $\dot{N}_{\rm GW} = 0.076$–0.095 yr^{-1} and those from BH-SN with $\dot{N}_{\rm GW} = 0.3$–0.36 yr^{-1} (see Table 3). Realistic $\dot{N}_{\rm GW}$ values will need the assessment of the GW to electromagnetic energy ratio which is necessarily smaller than unity from energy conservation.

ACKNOWLEDGMENTS

J.A.R. acknowledges the support by the International Cooperation Program CAPES-ICRANet financed by CAPES-Brazilian Federal Agency for Support and Evaluation of Graduate Education within the Ministry of Education of Brazil. M.K. and F.G.O. acknowledge the support given by the International Relativistic Astrophysics Erasmus Mundus Joint Doctorate Program under the Grants 2013–1471 and 2012–1710, respectively, from EACEA of the European Commission. M.M. and J.A.R. acknowledge partial support of the project No. 3101/GF4 IPC-11/2015, and the target program of the Ministry of Education and Science of the Republic of Kazakhstan. C.C. and S.F. acknowledge INdAM-GNFM for support.

REFERENCES

Abbott, B. P., Abbott, R., Abbott, T. D., et al. 2016, Living Reviews in Relativity, 19, arXiv:1304.0670
Allen, B., Anderson, W. G., Brady, P. R., Brown, D. A., & Creighton, J. D. E. 2012, Phys. Rev. D, 85, 122006
Anninos, P., Hobill, D., Seidel, E., Smarr, L., & Suen, W.-M. 1995, Phys. Rev. D, 52, 2044
Astone, P., Ballantini, R., Babusci, D., et al. 2006, Classical and Quantum Gravity, 23, S57
—. 2008, Classical and Quantum Gravity, 25, 114048
Becerra, L., Bianco, C. L., Fryer, C. L., Rueda, J. A., & Ruffini, R. 2016, ArXiv e-prints, arXiv:1606.02523
Becerra, L., Cipolletta, F., Fryer, C. L., Rueda, J. A., & Ruffini, R. 2015, ApJ, 812, 100
Belvedere, R., Boshkayev, K., Rueda, J. A., & Ruffini, R. 2014, Nucl. Phys. A, 921, 33
Berger, E. 2014, ARA&A, 52, 43
Bernuzzi, S., Dietrich, T., & Nagar, A. 2015a, Phys. Rev. Lett., 115, 091101
Bernuzzi, S., Nagar, A., Dietrich, T., & Damour, T. 2015b, Phys. Rev. Lett., 114, 161103
Bildsten, L., & Cutler, C. 1992, ApJ, 400, 175
Cadelano, M., Pallanca, C., Ferraro, F. R., et al. 2015, ApJ, 812, 63
Camp, J. B., & Cornish, N. J. 2004, Annual Review of Nuclear and Particle Science, 54, 525
Cipolletta, F., Cherubini, C., Filippi, S., Rueda, J. A., & Ruffini, R. 2015, Phys. Rev. D, 92, 023007
Davis, M., Ruffini, R., Press, W. H., & Price, R. H. 1971, Phys. Rev. Lett., 27, 1466
Davis, M., Ruffini, R., & Tiomno, J. 1972, Phys. Rev. D, 5, 2932
Detweiler, S. 1980, ApJ, 239, 292
Detweiler, S. L., & Szedenits, Jr., E. 1979, ApJ, 231, 211
Eichler, D., Livio, M., Piran, T., & Schramm, D. N. 1989, Nature, 340, 126
Finn, L. S., & Chernoff, D. F. 1993, Phys. Rev. D, 47, 2198
Flanagan, É. É., & Hughes, S. A. 1998, Phys. Rev. D, 57, 4535
Fryer, C. L., Oliveira, F. G., Rueda, J. A., & Ruffini, R. 2015, Phys. Rev. Lett., 115, 231102
Fryer, C. L., Rueda, J. A., & Ruffini, R. 2014, ApJ, 793, L36
Giacconi, R., & Ruffini, R., eds. 1978, Physics and astrophysics of neutron stars and black holes
Gizzi, D., & Rueda, J. A. 2016, to be submitted
Goodman, J. 1986, ApJ, 308, L47
Guetta, D., & Della Valle, M. 2007, ApJ, 657, L73
Guetta, D., Pian, E., & Waxman, E. 2011, A&A, 525, A53
Izzo, L., Rueda, J. A., & Ruffini, R. 2012, A&A, 548, L5
Kawaguchi, K., Kyutoku, K., Nakano, H., et al. 2015, Phys. Rev. D, 92, 024014
Klein, A., Barausse, E., Sesana, A., et al. 2016, Phys. Rev. D, 93, 024003
Kobayashi, S., & Mészáros, P. 2003, ApJ, 589, 861
Kovacevic, M., Izzo, L., Wang, Y., et al. 2014, A&A, 569, A108
Landau, L. D., & Lifshitz, E. M. 1975, The Classical Theory of Fields (Oxford: Pergamon Press)

Lazarus, P., Tauris, T. M., Knispel, B., et al. 2014, MNRAS, 437, 1485
Lee, W. H., Ramirez-Ruiz, E., & Page, D. 2004, ApJ, 608, L5
Liang, E., Zhang, B., Virgili, F., & Dai, Z. G. 2007, ApJ, 662, 1111
LIGO Scientific Collaboration, Aasi, J., Abbott, B. P., et al. 2015, Classical and Quantum Gravity, 32, 074001
Maggiore, M. 2007, Gravitational Waves. Vol. 1: Theory and Experiments (Oxford University Press)
Meszaros, P., & Rees, M. J. 1997, ApJ, 482, L29
Mirabel, I. F., & Rodríguez, L. F. 1998, Nature, 392, 673
Nagar, A., Damour, T., & Tartaglia, A. 2007, Classical Quantum Gravity, 24, S109
Narayan, R., Piran, T., & Shemi, A. 1991, ApJ, 379, L17
Paczynski, B. 1986, ApJ, 308, L43
Paschalidis, V., MacLeod, M., Baumgarte, T. W., & Shapiro, S. L. 2009, Phys. Rev. D, 80, 024006
Peters, P. C. 1964, Phys. Rev., 136, 1224
Peters, P. C., & Mathews, J. 1963, Phys. Rev., 131, 435
Rangel Lemos, L. J., Bianco, C. L., Mosquera Cuesta, H. J., Rueda, J. A., & Ruffini, R. 2010, in 25th Texas Symposium on Relativistic Astrophysics, 204
Rees, M., Ruffini, R., & Wheeler, J. A. 1974, Black holes, gravitational waves and cosmology (New York: Gordon and Breach Science Publishers Inc.)
Rhoades, C. E., & Ruffini, R. 1974, Physical Review Letters, 32, 324
Rigault, M., Aldering, G., Kowalski, M., et al. 2015, ApJ, 802, 20
Rodriguez, J. F., Rueda, J. A., & Ruffini, R. 2016, ArXiv e-prints, arXiv:1605.07609
Rosswog, S., Ramirez-Ruiz, E., & Davies, M. B. 2003, MNRAS, 345, 1077
Rueda, J. A., & Ruffini, R. 2012, ApJ, 758, L7
Ruffini, R., Bernardini, M. G., Bianco, C. L., et al. 2006, in The Tenth Marcel Grossmann Meeting, ed. M. Novello, S. Perez Bergliaffa, & R. Ruffini (Singapore: World Scientific), 369
Ruffini, R., Bernardini, M. G., & Bianco et al., C. L. 2008, in The Eleventh Marcel Grossmann Meeting, ed. H. Kleinert, R. T. Jantzen, & R. Ruffini, 368–505
Ruffini, R., Bianco, C. L., Fraschetti, F., Xue, S.-S., & Chardonnet, P. 2001, ApJ, 555, L117
Ruffini, R., Bernardini, M. G., Bianco, C. L., et al. 2007, in ESA Special Publication, Vol. 622, ESA Special Publication, 561
Ruffini, R., Wang, Y., Enderli, M., et al. 2015a, ApJ, 798, 10
Ruffini, R., Muccino, M., Kovacevic, M., et al. 2015b, ApJ, 808, 190
Ruffini, R., Rueda, J. A., Muccino, M., et al. 2016, ArXiv e-prints, arXiv:1602.02732
Shibata, M., & Taniguchi, K. 2011, Living Rev. Relat., 14
Soderberg, A. M., Kulkarni, S. R., Nakar, E., et al. 2006, Nature, 442, 1014
Sun, H., Zhang, B., & Li, Z. 2015, ApJ, 812, 33
Tauris, T. M., van den Heuvel, E. P. J., & Savonije, G. J. 2000, ApJ, 530, L93
Tauris, T. M., Kaspi, V. M., Breton, R. P., et al. 2015, Advancing Astrophysics with the Square Kilometre Array (AASKA14), 39
Virgili, F. J., Liang, E.-W., & Zhang, B. 2009, MNRAS, 392, 91
Virgili, F. J., Zhang, B., O'Brien, P., & Troja, E. 2011, ApJ, 727, 109
Wanderman, D., & Piran, T. 2010, MNRAS, 406, 1944
—. 2015, MNRAS, 448, 3026